1998 IEEE International Reliability Physics Symposium Proceedings, March 30 - April 2, 1998, pp. 26-35.

The Effect of Frequency on the Lifetime of a Surface Micromachined Microengine Driving a Load

Danelle M. Tanner, William M. Miller, William P. Eaton, Lloyd W. Irwin,
Ken A. Peterson, Michael T. Dugger, Donna C. Senft, Norman F. Smith, Paiboon Tangyunyong, and Samuel L. Miller

Sandia National Laboratories, P.O. Box 5800, MS 1081, Albuquerque, NM 87185-1081
email: tannerdm@sandia.gov

ABSTRACT

Experiments have been performed on surface micromachined microengines driving load gears to determine the effect of the rotation frequency on median cycles to failure. We did observe a frequency dependence and have developed a model based on fundamental wear mechanisms and forces exhibited in resonant mechanical systems. Stressing loaded microengines caused observable wear in the rotating joints and in a few instances lead to fracture of the pin joint in the drive gear.

INTRODUCTION

As MicroElectricalMechanical Systems (MEMS) become more commercially feasible, reliability studies and predictions will become crucial for its success. MEMS are typically classified into two types, sensors and actuators. There has been some reliability testing reported for sensors, [1,2] and specifically those that are exposed to harsh environments [3]. There has been little reliability work published on microactuators. Microactuators are used to drive many different types of devices from gear transmissions to pop-up mirrors [4,5]. The reliability of these MEMS devices is directly tied to the reliability of the microactuator. Actuator reliability based upon crack propagation in polysilicon was recently reported [6]. Recent data on the lifetime of the Sandia designed microengine was also reported [7].

The objective of this work was to determine the fundamental correlation between the operational drive frequency and the lifetime of the microengine. The comb drives of these microengines have springs which restore any deflections back to the rest position. The polysilicon comb drive exhibits a resonant frequency (the frequency of maximum displacement) like any mechanical oscillating system. By selecting frequencies above and below resonance, we have collected data for the median lifetime of the microengine driving a load as a function of f/f_o where f is the stress frequency and f_o is the resonance frequency . We have developed a predictive model for the number of revolutions to failure which is based on the fundamental principles of the physics of wear in a mechanically resonating system.

EXPERIMENTAL APPROACH

Lifetime Experiment

This study used the electrostatically driven microactuator (microengine) developed at Sandia National Laboratories [8]. The microengine consists of orthogonal linear comb drive actuators mechanically connected to a rotating gear as seen in Figure 1. By applying the proper drive voltages, the linear displacement of the comb drives was transformed into circular motion. The X and Y linkage arms are connected to the gear via a pin joint. The gear rotates about a hub which was anchored to the substrate. The microengine has been the focus of much investigation for MEMS devices experiencing

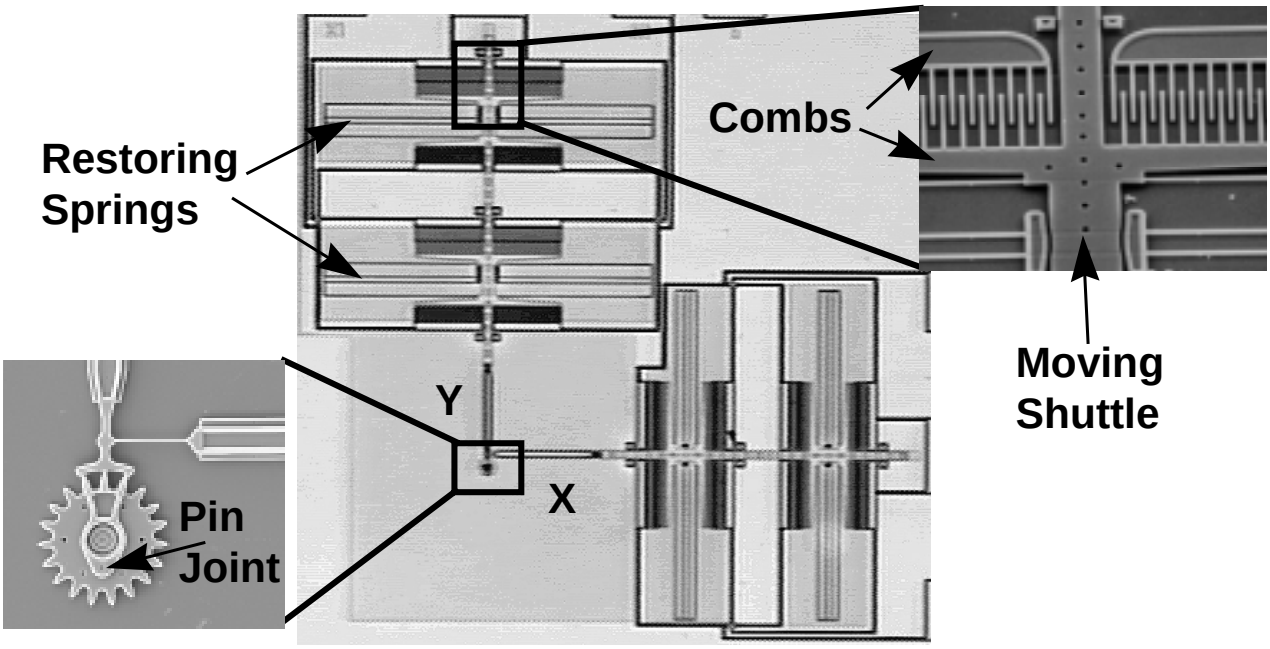

Figure 1. Sandia microengine with expanded views of the comb drive (top right) and the rotating gear (bottom left) shown in what we define as $\theta = 0$.

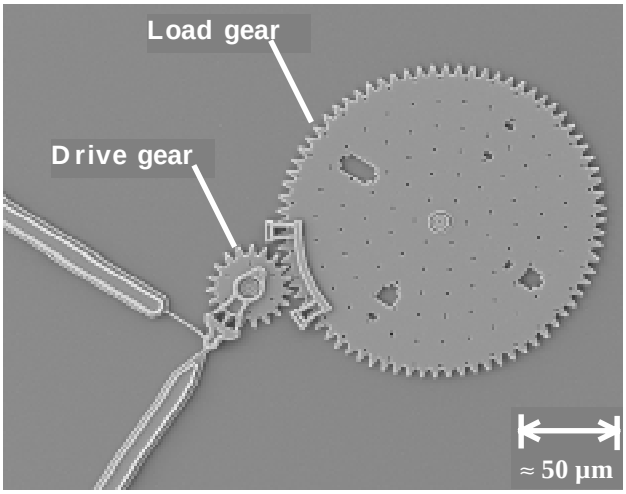

Figure 2a. The microengine drive gear shown with the load gear. The right bracket ( ]) shaped guide on the load gear mitigates out-of-plane wobble to ensure proper meshing of teeth.

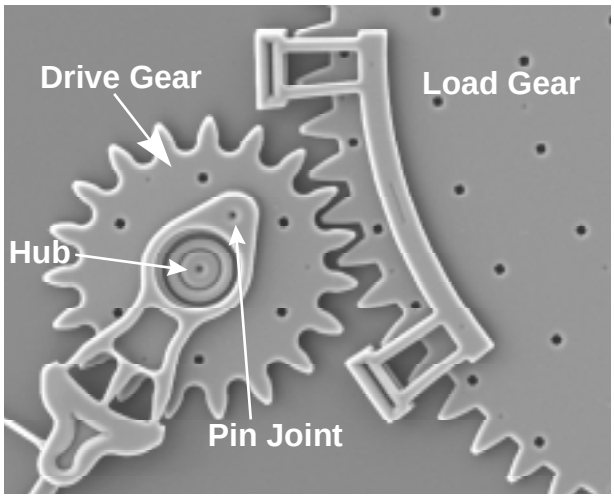

Figure 2b. Close-up view of the drive gear meshing with the load gear. The hub is anchored to the substrate and the pin joint connects the actuator linkage to the drive gear.

sliding friction [7,9].

We used the microengine to drive the load gear depicted in Figure 2a. A close-up view of the drive gear meshing with the load gear is shown in Figure 2b. The radius of the microengine drive gear was 38 µm and the load gear was four times as large. One of the many issues associated with the reliability of microengines is drive signal parameters [10]. If the drive signals fed to the comb drives are not optimized, there will be excessive forces on the hub and pin joint of the gear which will lead to early failures. We characterized the drive parameters fully by measuring both the resonant frequency and the normalized spring constant of the comb drives. They were 1720 Hz and 1875, respectively. For all experiments, we accelerated the load gear to full speed in three rotations of the drive gear. This method was necessary to account for the inertia of the large gear.

The die were packaged with glass covers to allow viewing of the rotating gears. The covers prevented particle contamination but allowed access to the ambient environment of the laboratory. The packages were stored in a dry nitrogen environment before the test. The tester, Sandia High Volume Measurement of Micromachine Reliability (SHiMMeR) [7], was used to provide electrical signals to large numbers of packaged microengines driving loads and to optically inspect them for functionality.

We performed stress tests at six frequencies, 860, 1204, 1500, 1720, 2408, and 3000 Hz. The resonant frequency of the comb drives was 1720 Hz which allowed for stresses both above and below resonance. The stress intervals followed roughly the same sequence for all the experiments. The sequence was 2000, 4000, 8000, 16000, …, rotation cycles of the drive gear per stress. If more than 4 parts failed during a particular stress, we repeated that stress interval. The devices were stressed at high speed and then slowed to 1 Hz to inspect for functionality. A failure was defined as the inability of the microengine drive gear to make a complete revolution at the 1 Hz inspection speed. During the inspection interval, we noted any observed changes or degradation in the motion of the gears for our records.

Wear Structure Experiment

To compare the worn surface morphology found in actual devices with that occurring under well-defined contact conditions, experiments were run on a specialized "sidewall" friction test device [11], shown in Figure 3. In this device, the sidewall of a beam having rectangular cross-section is brought into contact with the cylindrical surface of a vertical post using an electrostatic comb drive to apply a load force. A second electrostatic comb drive is used to reciprocate the beam against the post.

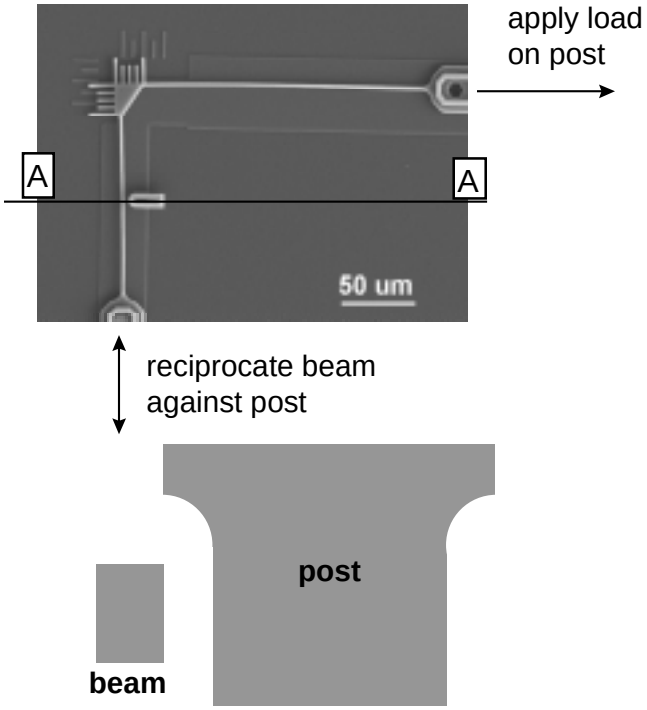

Figure 3. SEM micrograph showing the top view of the sidewall friction tester and a schematic cross-sectional view (A-A) of the contacting members.

Conditions in the experiments were chosen to duplicate as closely as possible the loading conditions found in the gear hubs of the microengine. The maximum force exerted by the drive linkage on the microengine gear was estimated to be 2.5 µN. Based on the geometry of the microengine, the peak Hertzian contact pressure assuming linear contact between the conformal polycrystalline silicon structural elements, and using an elastic modulus of 155 GPa and Poisson's ratio 0.23, was therefore 27 MPa at the gear hub and 140 MPa at the pin joint.

In this experiment, a normal force of 4 µN was applied between the beam and post resulting in a peak contact pressure of 144 MPa in

the sidewall device. The device was run at 127 Hz for a sliding distance of 10 m, equivalent to $1x10^6$ revolutions of the pin joint.

RESULTS

Data Analysis of Lifetime Experiment

Because the parts were observed at fixed inspection times, common to all the parts, the results fall into the category of reliability data called "interval" data. We plotted the accumulated number of cycles to failure against the cumulative percent failure for each stress frequency. The lognormal fit resulted in an estimate of t_{50}, the median cycles to failure. The estimate for the lognormal shape parameter, σ, was also determined.

The experimental results are listed in Table 1. We performed eight experiments and failed a total of 220 parts.

Table 1. Series of frequency experiments performed.

f (Hz)	f/f_o	# Parts on test	# Parts Failed	# stress intervals
860	0.5	34	28	30
1204	0.7	47	28	23
1500	0.87	9	9	21
1500	0.87	39	37	30
1720	1.0	25	25	30
2408	1.4	35	35	27
3000	1.74	15	14	23
3000	1.74	44	44	23

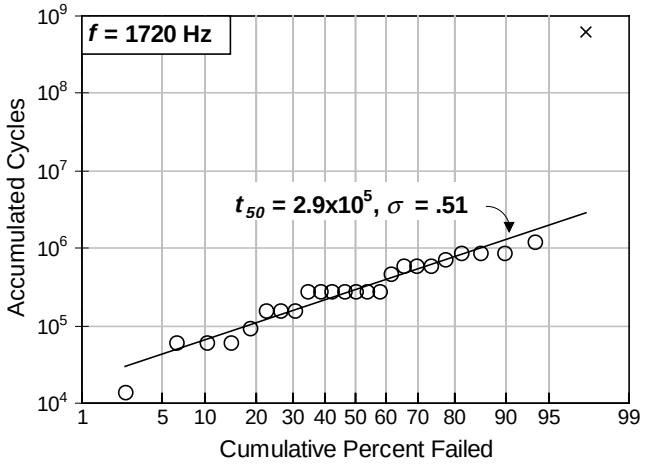

Figure 4. Lognormal distribution of accumulated cycles to failure for the resonant frequency stress. The freak data point marked by an x was omitted from the regression analysis.

Most of the data from each of the experiments could be described by a simple unimodal distribution such as seen in Figure 4. In this figure, the last point is roughly two orders of magnitude higher than the rest and was omitted from the fit. The regression analysis yielded a median cycles to failure of 2.9 x 10^5 cycles with σ = .51.

However, there were two cases where the distribution was bimodal. This occurred for stress frequencies of 860 and 2408 Hz. In these instances, we deconvoluted the data to determine the median cycles to failure for each population. Figure 5 shows the data with the upper and lower lines representing the two populations. The bimodal analysis using a separation fraction of 0.65 is also shown in the figure. Since the σs of both populations are similar, we believe that the underlying failure modes are the same, but that we have two populations, one of weak parts and the other of strong parts.

Table 2 has the results of lognormal fits to all of the frequency experiments. For the cases where we observed a bimodal distribution, the lower and upper t_{50} were presented. The data is also

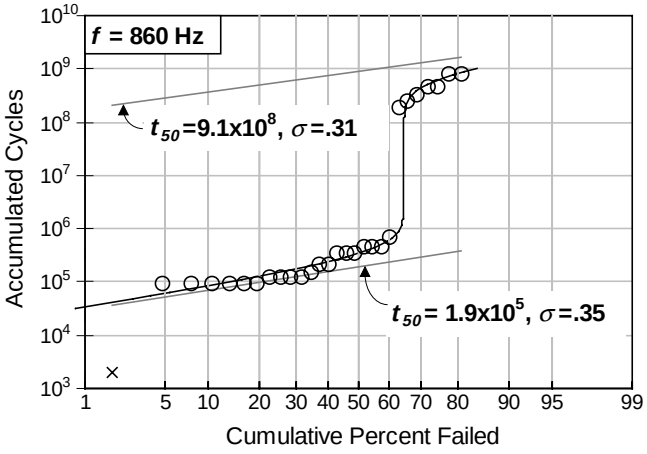

Figure 5. Lognormal probability plot for the 860 Hz test showing a bimodal distribution. The first data point (shown as x) was omitted from the deconvolution calculation.

Table 2. Results of median number of cycles to failure from all frequency experiments performed.

		Unimodal or Lower		Bimodal Upper	
f (Hz)	f/f_o	t_{50}	σ	t_{50}	σ
860	.5	$1.90x10^5$	.35	$9.08x10^8$	.31
1204	0.7	$2.91x10^5$	.28		
1500	0.87	$3.22x10^5$	.45		
1720	1.0	$2.90x10^5$	.51		
2408	1.4	$1.21x10^6$	.29	$2.49x10^8$	.32
3000	1.74	$1.29x10^6$	.70		

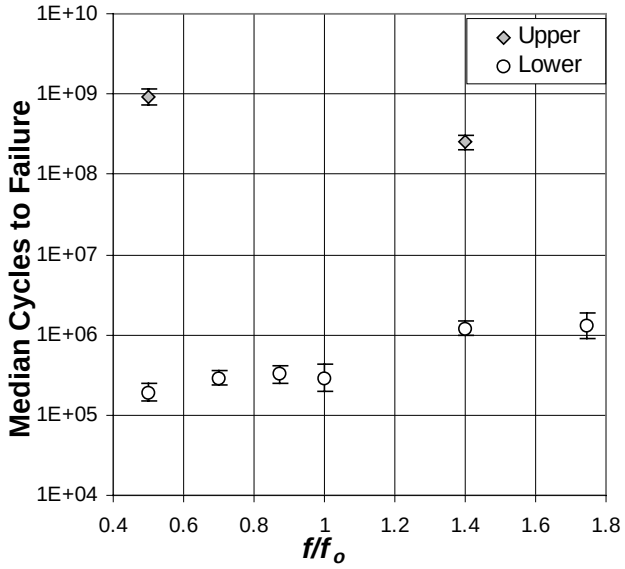

Figure 6. The frequency dependence of the lifetime of the micro-engines driving a load. The error bars represent 90% confidence bounds.

graphically represented in Figure 6 with 90% confidence bounds represented by error bars. As in the table, the unimodal distributions are grouped with the lower portion of the bimodal distribution. The upper portions of the bimodal distribution are only seen at two frequencies. These are extremely good microengines with lifetimes very close to the record of 7 billion cycles.

For the stress frequencies of 1500 and 3000Hz, we repeated the experiments and the results of the second experiment were within the 90% confidence bounds of the first experiment. We then averaged the two results. This was an excellent demonstration of lot to lot repeatability since the microengines in the second experiment were from a different fabrication lot but of the same technology and design.

Experimental Observations

The behavior of the microengines as they were stressed followed a consistent pattern. Initially the microengines ran smoothly. With the accumulation of stress, the operation of the microengines became sticky and jerky (stick-slip behavior) at inspection frequencies. Some of the microengines would actually work through the sticky behavior and become smooth again. Near the end of life, the rotation became more erratic until the microengine failed by sticking or rocking back and forth through a small angle. After failure, the part was still being stimulated by the drive signals so we optically panned across the entire microengine to get clues about the failure. We observed cases where the drive gear/load gear combination appeared stuck since we could see slight movement in the adjoining comb drives and shuttles. In other cases, the pin joint appeared to be stuck.

The lifetime behavior of the parts was markedly different for frequencies above and below resonance. Below resonance, the microengines initially operated smoothly at inspection and stress frequencies. With the accumulation of stress, the motion became jerky at the inspection frequency of 1 Hz, but was smooth at the higher frequency. The behavior at high frequencies was monitored using a strobe light to "slow down" the motion for visual inspection. Eventually, the motion of the gears froze at both inspection and stress frequencies.

Above resonance, the parts initially operated smoothly at inspection and stress frequencies. After some stress, they would start to chatter at stress frequencies; that is, the gears would vibrate at one position. This effect was greatest for the stress frequency of 3000Hz. We used a strobe light to observe the gear as it came up to high speed. The gears typically rotated smoothly for 10-15 seconds before the chatter began. At the onset of high speed chatter, the parts would still operate normally at inspection speed. Eventually, however, the motion of the gears froze at both inspection and stress frequencies.

Failure Analysis of Lifetime Experiment

Microengines driving loads tested to failure typically exhibited wear debris which was resolved optically. An example of this debris is shown in a SEM image in Figure 7. The left arrow in Figure 7 indicates a location where the debris has been moved out to the top surface of the hub on a drive gear. The right arrow indicates a site where debris can be seen in the gap between the vertical side walls of the drive gear and its hub.

Figures 8 and 9 show a result from a comparison of drive gears and load gears from several devices tested to failure. The light contrast debris is characteristically evident in the gap on the drive gear of Figure 8 and is characteristically absent in a similar gap from the load gear of Figure 9.

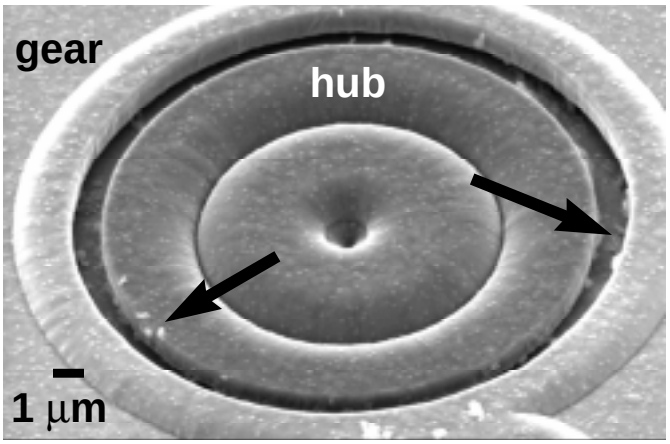

Figure 7. Top view SEM image of characteristic wear debris on drive gear and hub.

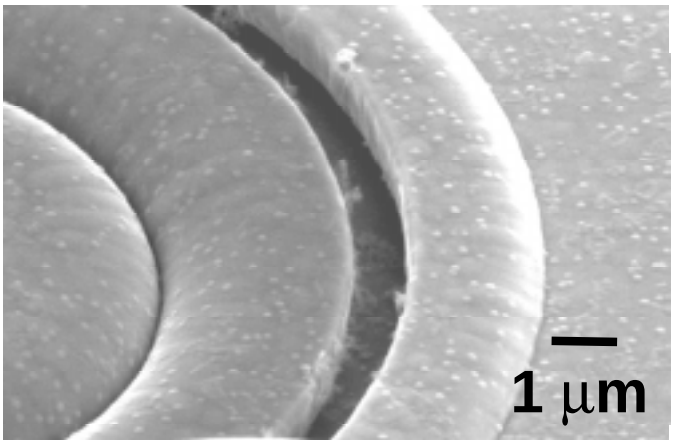

Figure 8. SEM image of gap between drive gear and hub showing characteristic accumulation of wear debris.

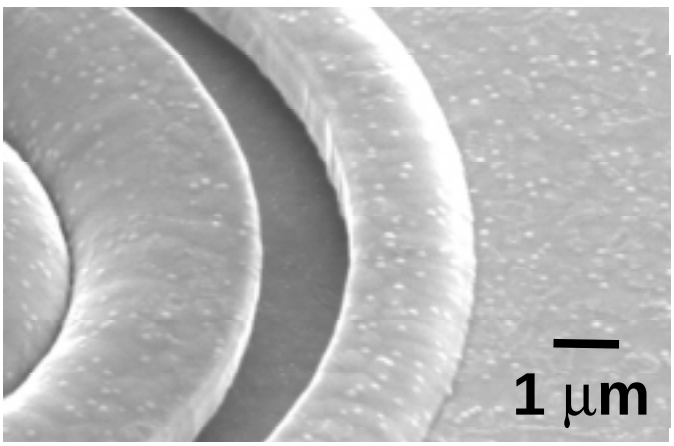

Figure 9. SEM image of gap between load gear and hub showing characteristic absence of wear debris.

Wear debris at drive pins has also been resolved optically in some cases when it is broadcast from beneath the drive arm. It can also be seen in the SEM by tilting the sample to look under the drive arm. Figure 10 shows such an image, where a broken pin has come to rest between the teeth of a gear. The debris covers the sidewall of the upper pin flange and has spread to a sidewall of the drive arm.

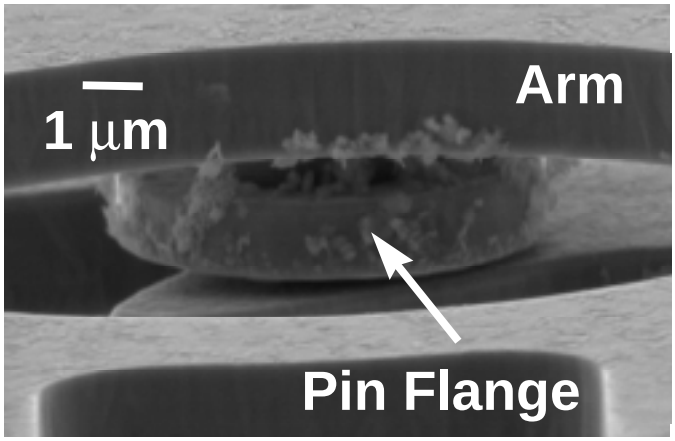

Figure 10. SEM image at high tilt angle which reveals wear debris adhering to the upper drive pin flange beneath the drive arm of a binary counter tested to failure due to pin breakage.

Severe drive pin wear and occasional breakage of drive pins was characteristic of these devices when tested to failure. An example of such wear is seen in Figure 11, where the bore of the hole in the drive gear which accepts the drive pin is shown after a pin has been broken. This wear has produced an out-of-round shape both by wearing material away and by depositing debris on the side wall of this hole. For comparison, a similar hole is shown in Figure 12 for a control sample with similar processing history which has not been tested. The view shown is from the bottom of the gear, but the bore of the hole is undamaged by wear. The particle at the left of the image is the result of breaking the pin during sample preparation.

Pin joint breakage was seen in 3 out of 220 microengines driving a load and only when the stress frequency was greater than the resonant frequency of 1720 Hz. Pin joint breakage was probably due to the coupling of the large inertial force of the load gear to the drive gear when it exhibits stick-slip behavior. This was the first observance of a stress failure in any microengine tested to date.

Wear debris was examined from a different perspective by using a conductive double adhesive laboratory tape to remove several gears and other components for examination of the undersides and the substrates from which they were removed. Figure 13 shows a SEM image from such a drive gear. The wear debris is attached to the sidewalls of the lower hub flange and the pin-retaining flange. It has radiated out from the perimeter of each of these flanges and has adhered to the bottom side of the drive gear. Gear teeth can be seen at the top of the image. This image was generated at 1 kV accelerating potential and shows interesting passive voltage contrast [12]. The dark contrast of the wear debris and the pin flange indicate that they are not grounded to the gear and are charging positively due to the 1 kV accelerating voltage. The pin flange and the hub flange by design must be free to move in the gear. The dark pin flange indicated pin join fracture during sample preparation. The dark contrast of the wear debris indicates that it is electrically insulating. Similar flanges from the load gear hub and from drive gears on engines which share processing history, but have not been run show pristine side walls which are free from such particles. The holes located concentric with the hub in Figure 13 are etch-release openings in the drive gear. The two dimples extend downward from the bottom of the gear to minimize the rubbing area in the event of contact with the substrate. No other evidence of wear has been observed at these dimples or any other surfaces on the gear or on the substrate beneath the gear. The dark circle in the center of the lower hub flange is the anchor point for the gear which was broken in order to obtain this view. It is darker than it's surroundings due to a resistance path between the point of illumination of the electron beam and the electrical ground provided by the gear and hub.

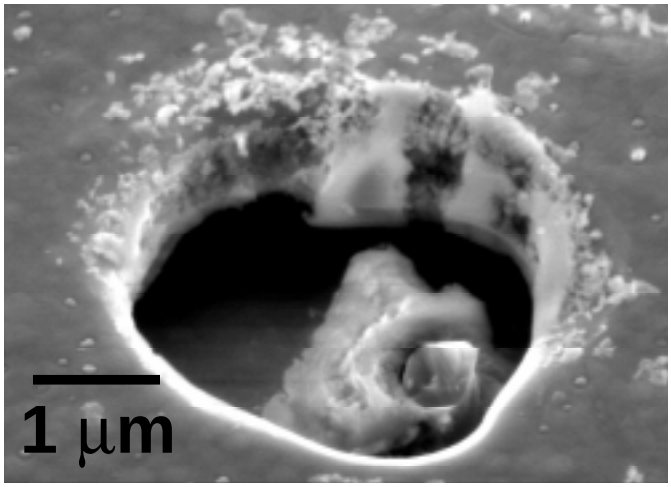

Figure 11. Severe pin hole damage in drive gear tested to failure (SEM).

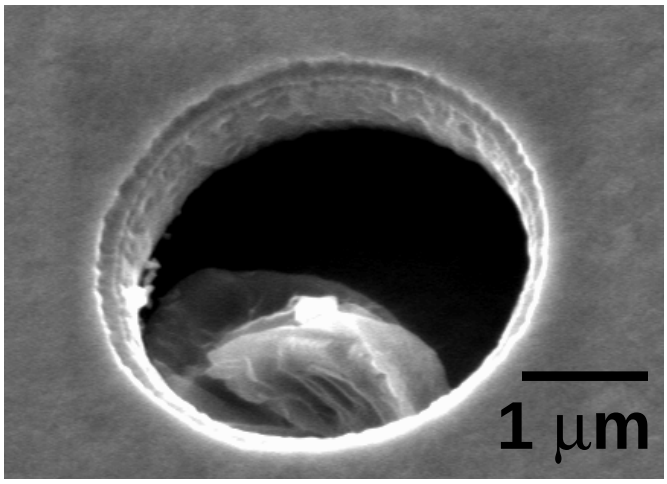

Figure 12. Undamaged side wall of pin hole in drive gear on control sample (SEM). This gear was not stressed.

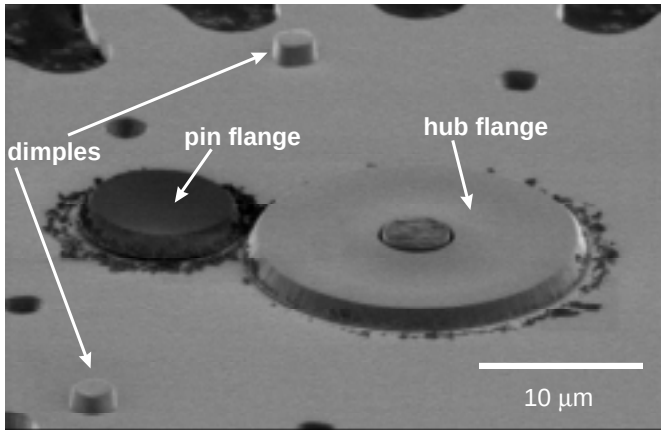

Figure 13. SEM image at 1kV showing wear debris on bottom of drive gear

A higher magnification image of the particles on a flange is shown in Figure 14. This SEM image was generated at 5 kV, and shows two size ranges for the wear debris seen at this location. Many of the particles are on the order of 50 nm in size and are elongated. A second size of feature are the rounder agglomerations of debris which are 200 nm and larger. Other agglomerations of wear debris have been observed which are submicron in size, but the mor-

phology has not been resolved distinctly at this time. This may be caused by the low density or perhaps, porosity which inhibits a high resolution image at the surface. The particles appear light in contrast due to negative charging from the 5 kV accelerating potential.

The images in Figure 15 show focused ion beam (FIB) cross sections for two samples with identical processing history. The upper image is from a control part which was not tested, and does not show any evidence of wear or other processing artifacts, while the lower image is from a part which was tested to failure in 480,000 cycles. The tested part shows abundant wear debris on bearing surfaces and surrounding areas as well as severe damage which reduced the minimum diameter of the pin. This circumferential notch on the pin concentrates subsequent stresses which is consistent with the result that broken pins typically show reduced diameters on both fracture surfaces.

Wear debris has also been observed on the shuttles and guides attached to the Y linkage arms. An example is shown in Figure 16. Although the debris lines up in this case, and can be seen to bridge the entire gap between shuttle and guide in Figure 17, it was not the reason for the shuttle being stuck in this position. This was shown when the flexible link between this shuttle and the engine was delicately severed with a xenon cutting laser, and the springs attached to the comb drive returned the shuttle to it's rest position.

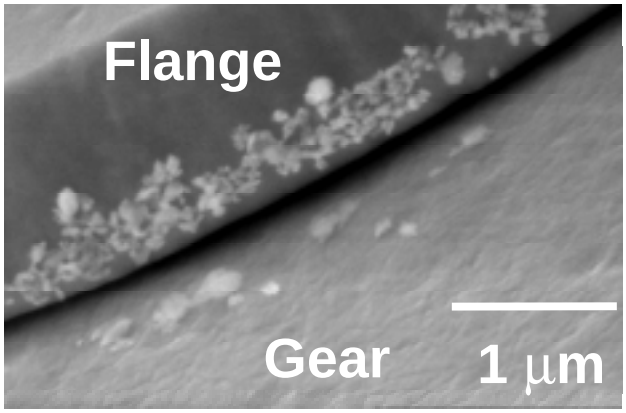

Figure 14. Wear particles a bearing surface flange on the underside of a drive gear.

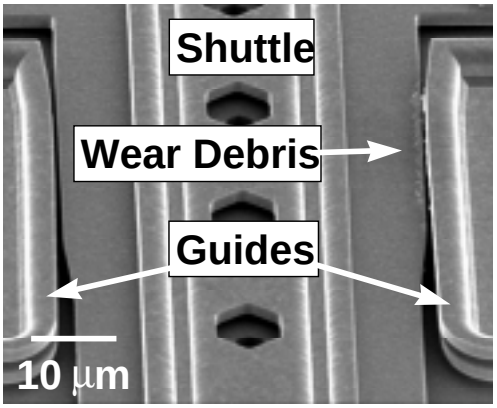

Figure 16. SEM image of wear debris on shuttle and guide.

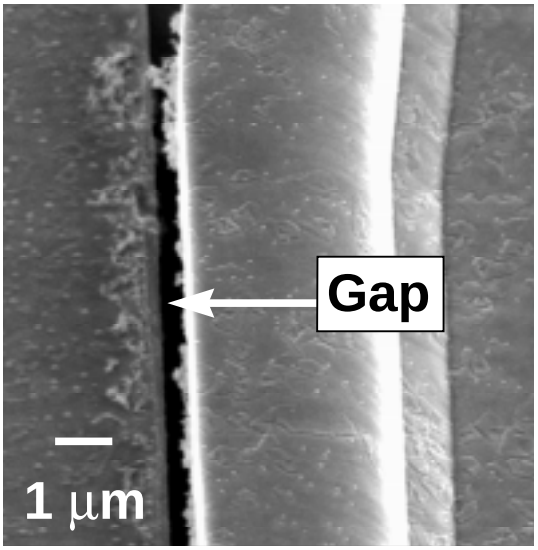

Figure 17. Higher magnification SEM view of debris at shuttle/guide location.

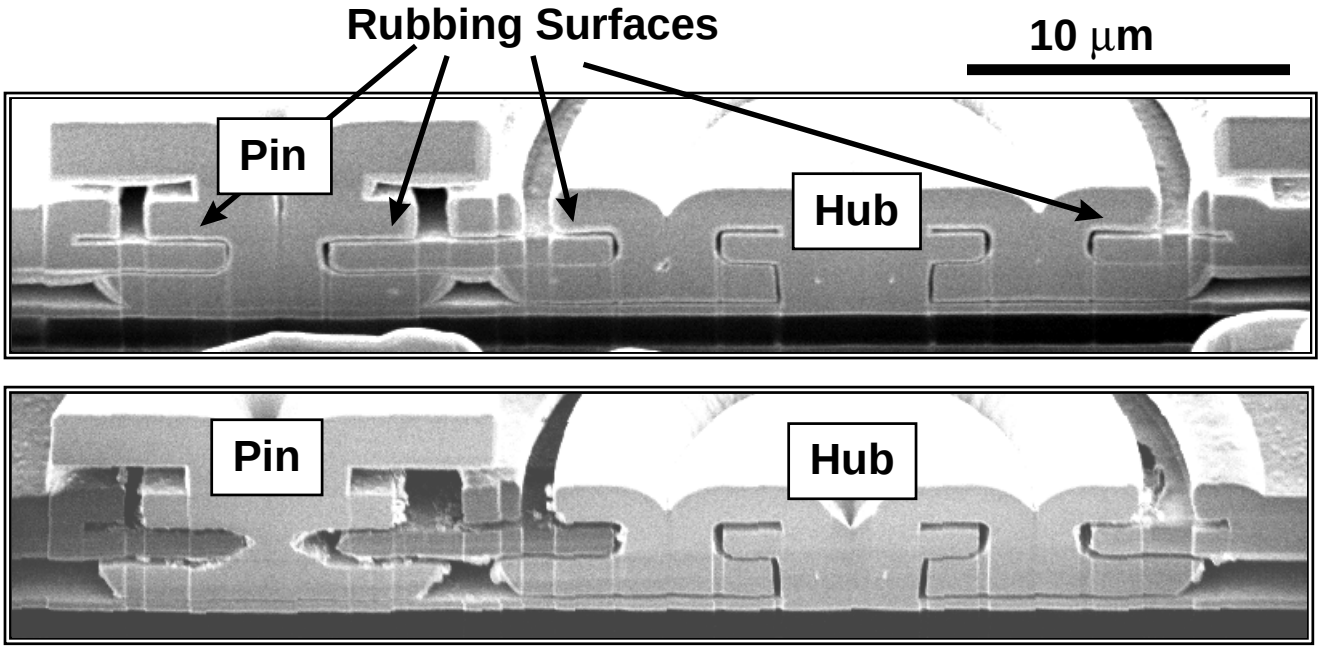

Figure 15. FIB cross sections of an engine which was not tested (above) and shows no wear debris, and an engine which was tested to failure in 480K cycles which shows severe wear on the pin joint and wear debris.

Data Analysis of Wear Structure Experiment

The results of the sliding wear test of the sidewall friction device are shown in Figures 18-19. The unworn surfaces shown in Figure 18 reveal smooth sidewall morphology for the cylindrical post where silicon is deposited into a hole etched in oxide. There are no visible particles or scratches on this silicon surface. The beam shown in Figure 18b was formed by reactive ion etching of silicon, and exhibits some texture due to the etching process. However, there are no attached particles or lateral scratches in the unworn side of the beam. Texture on the top surface of the silicon layers, in the form of small bumps, is inherent in the processing of the devices.

By comparison, the worn surfaces of the post and beam in Figure 19a and 19b show evidence of both attached particles and damage to the sliding surfaces. A scratch is evident near the top of the post in the micrographs of Figure 19a and 20a. The particles shown in Fig. 20a and 20b are agglomerates, roughly 200 nm in size, made up of much smaller particles on the order of tens of nanometers in size. The particles are collected at the entry and exit zone of the sliding contact on the vertical post.

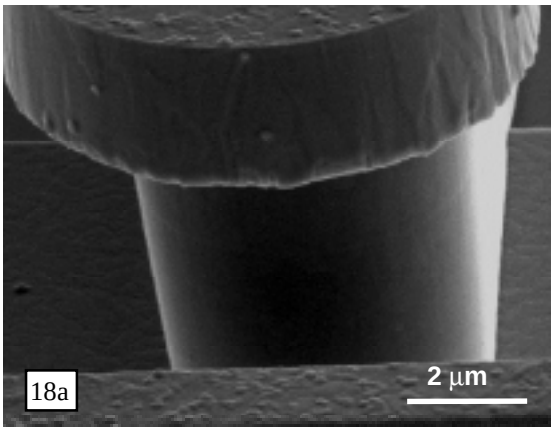

Figure 18a. SEM micrograph of the contacting surfaces in the sidewall device prior to testing showing the stationary cylindrical post.

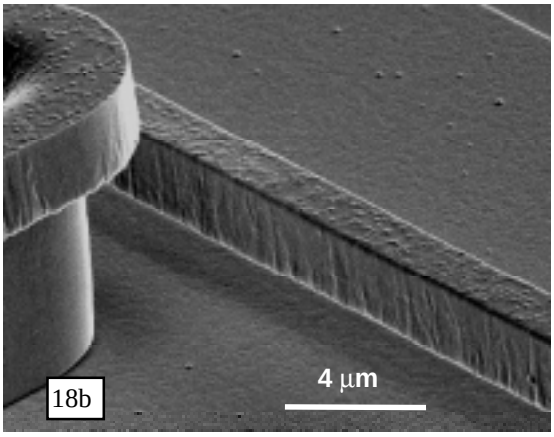

Figure 18b. SEM micrograph of the contacting surfaces in the sidewall device prior to testing showing the movable rectangular beam.

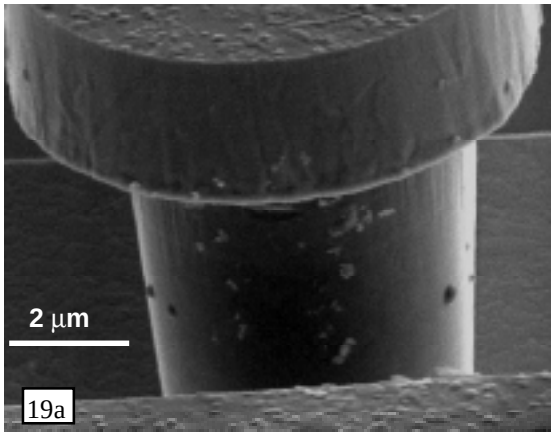

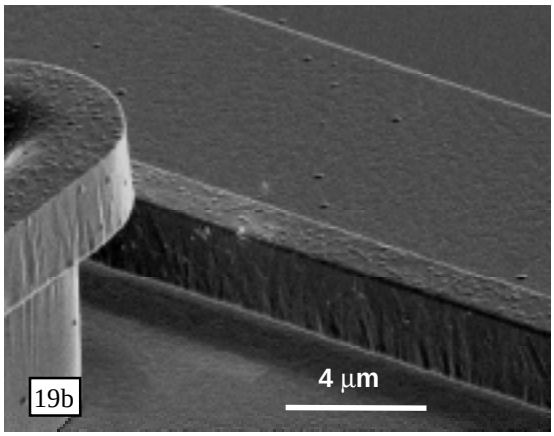

Figure 19. SEM micrographs of the sidewall device after reciprocation sliding for a total of 10 m at 140 MPa. Collections of wear particles are on the post surface in (a) and a few particles were collected on the beam surface in (b).

The surfaces in Figures 19 and 20 represent clear evidence of wear between the beam and post in the sidewall device, under contact conditions similar to those present in the microengine. The presence of wear particle agglomerates is expected in air, even though the wear process likely involves the initial removal of individual ~ 10 nm particles from the surface. After removal, individual wear particles are attracted to one another and the device surfaces by capillary and Van der Waals forces. The morphology of the particles alone is insufficient to determine whether they are generated by asperity-to-asperity adhesion followed by tensile fracture, by asperity fatigue due to cyclic stresses, or simply by abrasion of one surface by the other. In fact, the wear process likely involves a combination of these mechanisms, such that surface degradation and adhesion or fatigue is responsible for creating the initial wear particles, and particles trapped at the interface during sliding result in abrasion to create additional wear particles. Experiments to investigate the evolution of debris size and morphology during sliding at these conditions is needed to determine the wear mechanism, and is the subject of additional work.

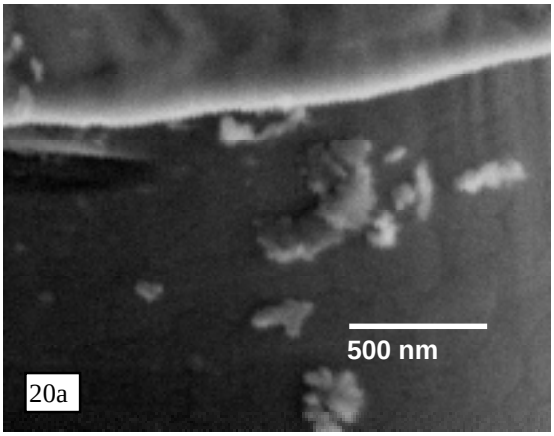

Figure 20a. Magnified images of particles on the post are shown.

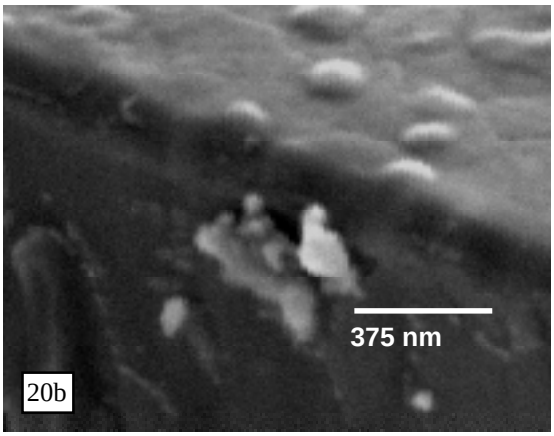

Figure 20b. Magnified images of particles on the beam are shown.

DISCUSSION

Failure Model: Types of Failures

There are seven primary wear failure mechanisms observed for macroscopic mechanical systems [13]: adhesion, abrasion, corrosion, surface fatigue, deformation, impact and fretting wear. Due to the microscopic nature of each of these mechanisms, we would expect that one of them (as opposed to some other mechanism) would be responsible for the wear-out of the micromachines studied in this paper.

During these experiments, neglible radial force was applied to drive these gears along with 3 μN of tangential force. At forces above approximately 4 μN the nature of the frictional forces in these engines is known to change abruptly [9] and result in observable wear tracks [11] characteristic of abrasive wear [13]. No wear tracks were expected nor evident during these tests.

There was no evidence of corrosion by-products, ruling this wear mechanism out. Finally, surface fatigue, deformation and impact wear typically require forces in excess of those for abrasive wear. Again such forces were not applied. Fretting wear occurs where machine elements experience fluctuating loads, leading to microcracks and ultimately failure by fatigue. Microcracks have not been observed.

Adhesive Failure Model

Although a combination of wear mechanisms would probably provide the most complete model, we propose adhesive wear as the most likely prevalent mechanism responsible for failure in these micromachines. Adhesive wear occurs when contact of asperities between two solid bodies (Figure 21a) leads to plastic flow and cold welding (Figure 21b). The asperity then tears away, leaving a particle transferred to one surface (Figure 21c). In this way, material can transfer from one surface to another and result in regions where the micromachine can begin to catch and then fail, as observed.

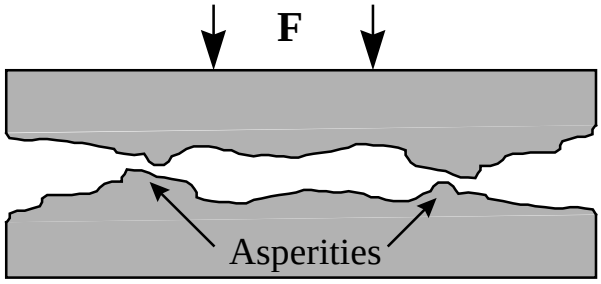

Figure 21a. Force F_r brings the two surfaces into contact at the asperities.

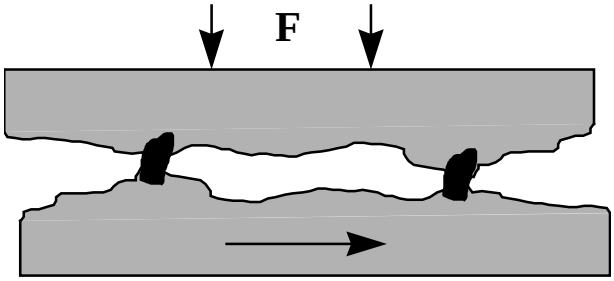

Figure 21b. As the lower surface moves the asperities cold weld together.

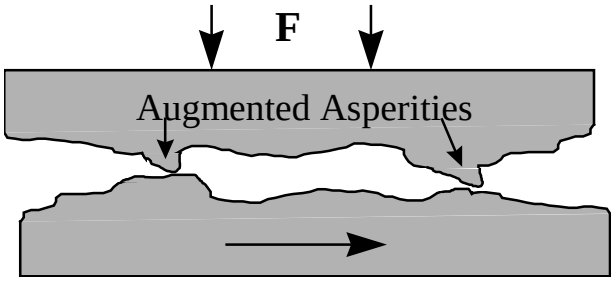

Figure 21c. As the lower surface continues to move, the metal breaks free again, leading to the augmented asperities on the upper surface.

The derivation of the model for adhesive failure begins by assuming that there is some critical volume, V_c , of material that must be transferred in order to stop the motion of the micromachine. We anticipate that V_c is not a single number but is a distribution of values.

In adhesive wear, the relationship between the wear volume ΔV, and the length of the motion producing the wear, ΔL is given as [13]:

$$\Delta V = \Delta L\left(\frac{KF}{9\sigma_{yp}}\right) \quad (1)$$

where K is the adhesive wear constant
F is the force on the joint and
σ_{yp} is the uniaxial yield strength

The total length of the motion creating the wear is then related to the radius of the joint, *r*, and the number of revolutions, *R*, that the engine makes by:

$$\Delta L = 2\pi r R \tag{2}$$

Bringing equations (1) and (2) together, setting ΔV to V_c, the critical volume for failure and R to R_f, the number of revolutions to failure and solving for R_f we get:

$$R_f = \left(\frac{9}{2\pi}\right)\left(\frac{\sigma_{yp}}{K}\right)\frac{V_c}{rF} \tag{3}$$

The true force on the joint will vary with excitation frequency, ω, as the critical frequency, ω_o , for resonance is approached provided that either the drive signal is a pure sine wave (which it is not) or is a custom signal intended to account for inertial effects (which it is) but applied to a system that has some play in the joints. The joints have approximately 50% tolerance as measured by the total diametral gap divided by the joint size.

In such a case, the net force on the joint will increase as the frequency approaches the critical frequency as [14]:

$$F = F_n\left[\frac{1}{\sqrt{\left[1-\left(\frac{\omega}{\omega_o}\right)^2\right]^2+\left(\frac{1}{Q}\frac{\omega}{\omega_o}\right)^2}}\right] \tag{4}$$

where the term in large square brackets represents a "magnification factor" caused by approach to resonance and

F_n is the nominal force applied to the joint,

Q is the "quality factor" of the damped harmonic mechanical system and

ω / ω_o is the ratio of the driving frequency to the resonant frequency of the system.

Combining equations (3) and (4) we now arrive at the complete description for the reliability of a MEMS actuator failing due to adhesive wear, where again R_f represents the median number of revolutions to failure.

$$R_f = \left(\frac{9}{2\pi}\right)\left(\frac{\sigma_{yp}}{K}\right)\frac{V_c}{rF_n}\left[\sqrt{\left[1-\left(\frac{\omega}{\omega_o}\right)^2\right]^2+\left(\frac{1}{Q}\frac{\omega}{\omega_o}\right)^2}\right]$$

Note that there are no adjustable parameters. All values are either physical constants that are material dependent and known or have been measured or set in running the experiment. Table 3 has the values of the model parameters and the corresponding references. Even V_c, the critical volume of adhered material, can be estimated from known physical parameters (see Appendix).

Comparison of the Failure Model to the Data

In order to confirm the model, derived above, we compare it to the actual failure data for the unimodal or lower distributions given in Table 2. This comparison is shown in Figure 22. We disregard the point at the highest frequency since we know that the failure mechanism was different because of the high speed chatter. The lower dashed line is the shape that we get by simply using our best estimates of the physical parameters (from Table 3) in equation 5. The upper solid line modifies the value of K to be $1.1\text{x}10^{-7}$. Values of K for adhesive wear range over orders of magnitude in the literature [15]. Our value for Q in Table 3 was measured using a micro-engine driving a load gear. The Q factor in the model determines the shape of the curve. The effect of a smaller Q does two things, a) shift the minimum to lower frequencies and b) reduce the V-shape in the curve. Both of these effects were seen in the data.

Note three important characteristics in the data versus model comparison:

1) the functional dependence is correct, with the model clearly predicting the decrease in the number of revolutions to failure around the resonant frequency,

2) the significant increase in the number of revolutions to failure above resonant frequency and

3) the overall scale of the predicted number of revolutions to failure, based solely on physical parameters.

Table 3. Failure Model Parameters

Variable	Parameter	Value	Ref.
σ_{yp}	uniaxial yield strength	$1.2\text{x}10^{-3}$ N/μm^2	[16]
K	adhesive wear constant	$5\text{x}10^{-7}$	[15]
V_c	critical volume	~$1.25\text{x}10^{-4}$ μm^3	Appendix
r	pin joint radius	1μm	measured
F_n	applied force	$3\text{x}10^{-6}$ N	[9]
ω_o	resonant freq.	1720 Hz	measured
Q	quality factor	2.2	measured

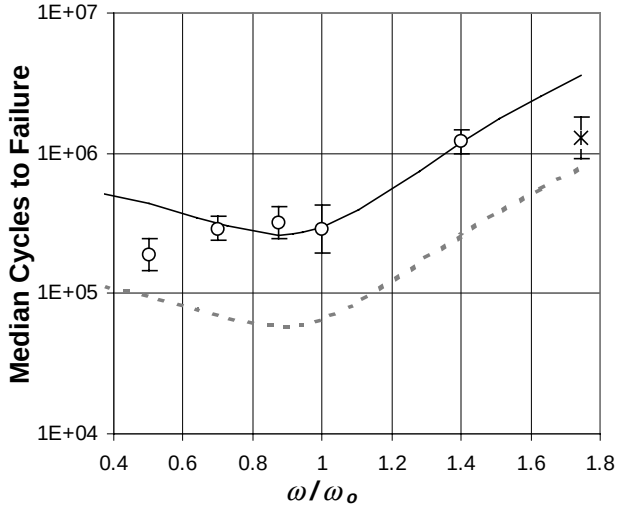

Figure 22. Comparison of failure data to the proposed adhesive wear model. The dashed line represents the model using $K = 5\text{x}10^{-7}$. The value of $K = 1.1\text{x}10^{-7}$ was used in the model to generate the solid line.

CONCLUSIONS

We have presented and validated the first quantitative and predictive model for MEMS actuator reliability. Statistically significant data over a wide range of frequencies both above and below resonance are accurately described by this first principles model. No adjustable parameters are needed. The model, which is based on the concept of wear coupled with mechanical resonant effects correctly describes both our qualitative and quantitative observations of wear.

Experimental reproducibility was demonstrated across different lots within the same technology. Our results are therefore valid for this technology and may be generally valid for surface micromachined polysilicon-based actuator reliability.

One of the critical unmeasured constants in our model is *K*, the adhesive wear constant. To further validate this model, a good measure of *K* will be needed.

The large amounts of debris we observed in the areas of rubbing surfaces led to the failures in the drive gears of the microengines as detailed in numerous SEM images. Wear morphology observed in the pin joints was successfully duplicated in simpler structures driven under similar conditions. The FIB cross sections of the drive gear showed severe notching in the pin joint which probably lead to eventual breakage of the pin joint in 3 of the 220 parts stressed.

The results from the sidewall structure indicate that both adhesive and abrasive wear was apparent at these forces. Therefore, a more complete model may have to take additional wear mechanisms into account.

APPENDIX

The critical volume, V_c, is a measure of the total amount of material that must be transferred by adhesive wear before a failure can occur. This is an unknown quantity. However, we have estimated it by calculating the size of asperity needed to stop the motion of the joint after a cold weld occurs, as in Figure 6b. The cross-sectional area of such a weld that can just stop the motion of the joint is given as:

$$A_c = F_n / \sigma_{yp} \tag{6}$$

where A_c is the "critical area" of the cold weld.

If one assumes a roughly cubic mass of material with this critical area, then the critical volume of this mass is given by:

$$V_c = A_c^{3/2} = \left[F_n / \sigma_{yp}\right]^{3/2} \tag{7}$$

Which for the values of force and yield strength in table 1, give a value of $1.25 \times 10^{-4}\ \mu m^3$.

ACKNOWLEDGMENTS

The authors thank the personnel of the Microelectronics Development Laboratory at SNL for fabricating, releasing, and packaging the devices used for this test. Special thanks to Peggy Clews and Heather Schriner who were instrumental in providing enough parts for this large experiment. We also acknowledge the help of Karen Helgesen for acquiring the data and Alex Pimental for the FIB cuts.

Sandia is a multiprogram laboratory operated by Sandia Corporation, a Lockheed Martin Company, for the United States Department of Energy under contract DE-AC04-94-AL85000

REFERENCES

[1] S. Bart, J. Chang, T. Core, L. Foster, A. Olney, S. Sherman, W. Tsang, "Design Rules for a Reliable Surface Micromachined IC Sensor", *1995 IEEE International Reliability Physics Proceedings, IRPS 95*, pp. 311-317 (1995).

[2] S. Cunningham, "Reliability and Quality Assurance of MEMS Technology", *Micromachining Workshop III, Abstracts*, (Sept. 1996).

[3] T. Maudie, "Testing Requirements and Reliability Issues Encountered with Micromachined Structures", *Proceedings Of 2nd International Conference on Microstructures and Microfabricated Systems"*, **95-27**, 1995, pp. 223-230.

[4] J. J. Sniegowski, "Multi-level polysilicon surface-micromachining technology: applications and issues," *Proceedings of the ASME Aerospace Division,* **Vol. 52**, , 1996, pp. 751-759.

[5] http://www.mdl.sandia.gov/Micromachine/

[6] S.B. Brown, "Materials Reliability in MEMS Devices", *Technical Digest, 1997 International Conference of Solid-State Sensors and Acuators, Transducers '97*, pp. 591-593.

[7] D. M. Tanner, N. F. Smith, D. J. Bowman, W. P. Eaton, K. A. Peterson, " First Reliability Test of a Surface Micromachined Microengine Using SHiMMeR," *Proceedings SPIE Symposium on Micromachining and Microfabrication,* **Vol. 3224**, Austin, 1997, pp 14-23.

[8] E. J. Garcia and J. J. Sniegowski, "Surface micromachined microengine", Sensors and Actuators A, **Vol. 48**, 1995, pp. 203-214.

[9] S. L. Miller, J. J. Sniegowski, G. LaVigne, and P. J. McWhorter, "Friction in Surface Micromachined Microengines", *Proceedings of SPIE Smart Electronics and MEMS* **Vol. 2722**, San Diego, Feb. 28-29, 1996, pp. 197-204.

[10] S. L. Miller, J. J. Sniegowski, G. LaVigne, and P. J. McWhorter, "Performance tradeoffs for a surface micromachined microengine", *Proceedings of SPIE Micromachined Devices and Components II*, **Vol. 2882**, Austin, October. 14-15, 1996, pp. 182-191.

[11] D. C. Senft and M. T. Dugger, " Friction and wear in surface micromachined tribological test devices," *Proceedings SPIE Symposium on Micromachining and Microfabrication,* **Vol. 3224**, Austin, 1997, pp 31-38.

[12] K. A. Peterson, P. Tangyunyong, and D. L. Barton, "Failure Analysis for Micro-Electrical-Mechanical Systems (MEMS)," *Proceedings of the 23rd International Symposium for Testing and Failure Analysis*, October 1997, Santa Clara, pp. 133-142.

[13] J. A. Collins, *Failure of Materials in Mechanical Design*, New York,: John Wiley & Sons, 1981.

[14] C. R. Freberg and E. N. Kemler, *Elements of Mechanical Vibration, 2nd ed.*, New York, John Wiley & Sons, Inc., 1949.

[15] Ernest Rabinowicz, *Friction and Wear of Materials*, 2nd ed., New York, John Wiley & Sons, Inc., 1995.

[16] W. N. Sharpe, Jr, B. Yuan, R. Vaidyanathan and R. L. Edwards, "Measurements of Young's Modulus, Poisson's Ratio and Tensile Strength of Polysilicon," *Proc. MEMS 97, 10th IEEE Inter. Workshop on MicroElectroMechanical Systems*, pp. 424-429.